

000
001
002
003
004
005
006
007054
055
056
057
058
059
060
061
062
063
064
065
066
067
068
069
070
071
072
073
074
075
076
077
078
079
080
081
082
083
084
085
086
087
088
089
090
091
092
093
094
095
096
097
098
099
100
101
102
103
104
105
106
107

SHS-Net: Learning Signed Hyper Surfaces for Oriented Normal Estimation of Point Clouds

Anonymous CVPR submission

Paper ID 722

Abstract

We propose a novel method called SHS-Net for oriented normal estimation of Point Clouds by learning signed hyper surfaces, which can accurately predict normals with global consistent orientation from various point clouds. Almost all existing methods estimate oriented normals through a two-stage pipeline, i.e., unoriented normal estimation and normal orientation, and each step is implemented by a separate algorithm. However, previous methods are sensitive to parameter settings, resulting in poor results from point clouds with noise, density variations and complex geometries. In this work, we introduce signed hyper surfaces (SHS), which are parameterized by multi-layer perceptron (MLP) layers, to learn to estimate oriented normals from point clouds in an end-to-end manner. The signed hyper surfaces are implicitly learned in a high-dimensional feature space where the local and global information is aggregated. Specifically, we introduce a patch encoding module and a shape encoding module to encode a 3D point cloud into a local latent code and a global latent code, respectively. Then, an attention-weighted normal prediction module is proposed as a decoder; which takes the local and global latent codes as input to predict oriented normals. Experimental results show that our SHS-Net outperforms the state-of-the-art methods in both unoriented and oriented normal estimation on the widely used benchmarks. The code, data and pretrained models will be publicly available.

1. Introduction

In computer vision and graphics, estimating normals for point clouds is a prerequisite for many techniques. As an important geometric property of point clouds, normals with consistent orientation, i.e., *oriented normals*, clearly reveal the geometric structures and make significant contributions in downstream applications, such as rendering and surface reconstruction [24–26]. Generally, the estimation of oriented normals requires a two-stage paradigm (see Fig. 1):

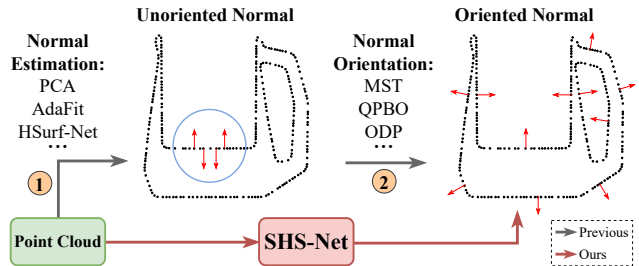


Figure 1. We propose SHS-Net to estimate oriented normals directly from point clouds. In contrast, previous studies usually achieve this process through a two-stage paradigm using different algorithms, i.e., (1) unoriented normal estimation (e.g., PCA [19], AdaFit [58] and HSurf-Net [32]) and (2) normal orientation (e.g., MST [19], QPBO [44] and ODP [37]).

(1) the unoriented normal estimation from the local neighbors of the query point, (2) the normal orientation to make the normal directions to be globally consistent, e.g., facing outward of the surface. While unoriented normals can be estimated by plane or surface fitting of the local neighborhood, determining whether the normals are facing outward or inward is ambiguous. In recent years, many excellent algorithms [5, 29, 31, 32, 58] have been proposed for unoriented normal estimation, while there are few methods that have reliable performance for normal orientation or directly estimating oriented normals. Estimating oriented normals from point clouds with noise, density variations, and complex geometries in an end-to-end manner is still a challenge.

The classic normal orientation methods rely on simple greedy propagation, which selects a seed point as the start and diffuses its normal orientation to the adjacent points via a minimum spanning tree (MST) [19, 27]. These methods are limited by error accumulation, where an incorrect orientation may degenerate all subsequent steps during the iterative propagation. Furthermore, they heavily rely on a smooth and clean assumption, which makes them easily fail in the presence of sharp edges or corners, density variations and noise. Meanwhile, their accuracy is sensitive to the neighborhood size of propagation. For example, a large size is usually used to smooth out outliers and noise, but can also

108 erroneously include nearby surfaces. Considering that local
109 information is usually not sufficient to guarantee robust orien-
110 tation, some improved methods [22, 37, 44, 45, 48, 52] try
111 to formulate the propagation process as a global energy opti-
112 mization by introducing various constraints. Since their
113 constraints are mainly derived from local consistency, the
114 defects are inevitably inherited, and they also suffer from
115 cumulative errors. Moreover, their data-specific parameters
116 are difficult to generalize to new input types and topologies.
117

118 Different from the propagation-based methods, which
119 only consider the adjacent orientation, the volume-based
120 approaches exploit volumetric representation, such as
121 signed distance functions [34, 39] and variational formula-
122 tions [2, 21, 47]. They aim to divide the space into inter-
123 ior/exterior and determine whether point normals are fac-
124 ing inward or outward. Despite improvements in accu-
125 racy and robustness, these methods cannot scale to large
126 point clouds due to their computational complexity. In
127 general, propagation-based methods have difficulty with sharp
128 features, while volume-based methods have difficulty with
129 open surfaces. Furthermore, the above-mentioned meth-
130 ods are usually complex and require a two-stage operation,
131 their performance heavily depends on the parameter tuning
132 in each separated stage. Recently, several learning-based
133 methods [17, 18, 49] have been proposed to deliver oriented
134 normals from point clouds and have exhibited promising
135 performance. Since they focus on learning an accurate local
136 feature descriptor and do not fully explore the relationship
137 between the surface normal orientation and the underlying
138 surface, their performance cannot be guaranteed across dif-
139 ferent noise levels and geometric structures.
140

141 In this work, we propose to estimate oriented normals
142 from point clouds by implicitly learning *signed hyper sur-*
143 *faces*, which are represented by MLP layers to interpret the
144 geometric property in a high-dimensional feature space. We
145 learn this new geometry representation from both local and
146 global shape properties to directly estimate normals with
147 consistent orientation in an end-to-end manner. The insight
148 of our method is that determining a globally consistent nor-
149 mal orientation should require global context to eliminate
150 the ambiguity from local since orientation is not a local
151 property. We evaluate our method by conducting a series of
152 qualitative and quantitative experiments on a range of point
153 clouds with different sampling densities, noise levels, thin
154 and sharp structures.
155

156 Our main contributions can be summarized as follows.
157

- 158 • We introduce a new technique to represent point cloud
159 geometric properties as signed hyper surfaces in a high-
160 dimensional feature space.
161 • We show that the signed hyper surfaces can be used to es-
timate normals with consistent orientations directly from
point clouds, rather than through a two-stage paradigm.
• We experimentally demonstrate that our method is able

162 to estimate normals with high accuracy and achieves the
163 state-of-the-art results in both unoriented and oriented
164 normal estimation.
165

2. Related Work

2.1. Unoriented Normal Estimation

166 Over the past few decades, many algorithms have
167 been proposed for point cloud normal estimation, such
168 as the classic Principle Component Analysis (PCA) [19]
169 and its improvements [1, 20, 28, 38, 42], Voronoi-based
170 paradigms [2, 3, 13, 35], and variants based on complex sur-
171 face [4, 10, 16, 30, 40]. These methods are usually sensitive
172 to noise and have limited accuracy even with heavy fine-
173 tuned parameters. More recently, learning-based methods
174 have been proposed to improve performance in this area and
175 can be mainly divided into two categories: regression-based
176 and surface fitting-based. The regression-based methods try
177 to directly predict normals from structured data [8, 33, 43]
178 or raw point clouds [6, 17, 18, 32, 54–56] in a data-driven
179 manner. Among them, HSurf-Net [32] achieves good per-
180 formance by learning hyper surfaces from local patches, but
181 the learned surfaces cannot determine the normal orienta-
182 tion without global information. The surface fitting-based
183 methods integrate the traditional surface fitting techniques,
184 such as plane fitting [9, 29] and jet fitting [5, 31, 53, 57, 58],
185 into the end of the learning pipeline. They usually carefully
186 design a network to predict point-wise weights, and then
187 use a weighted surface formulation to solve the fitted sur-
188 face normal. The normals estimated by the above methods
189 randomly face both sides of the object surface and cannot
190 be directly used in many downstream applications without
191 normal orientation.
192

2.2. Consistent Normal Orientation

193 To make the unoriented normals have consistent ori-
194 ntations, early approaches mainly focus on local consisten-
195 cy and use the orientation propagation strategy upon a mini-
196 mum spanning tree (MST) to let the adjacent points have
197 the same orientations, such as the pioneering work of [19]
198 and its improved methods [22, 44, 45, 48, 52]. These methods
199 have many limitations in real applications as we introduced
200 earlier. ODP [37] aims to achieve global consistency by
201 introducing a dipole propagation strategy across the parti-
202 tioned patches, but its robustness may suffer from the patch
203 partition. On the contrary, some alternative approaches
204 propose to solve the consistent normal orientation through
205 volumetric representation. They are usually developed for
206 reconstructing surfaces from unoriented points by various
207 techniques, such as signed distance functions [34, 39], vari-
208 ational formulations [2, 21, 47], visibility [11, 23], isovalue
209 constraints [50] and active contours [51]. Recently, a
210 few works [17, 18, 49] explore to predict oriented normals
211 [212, 213, 214, 215].
216

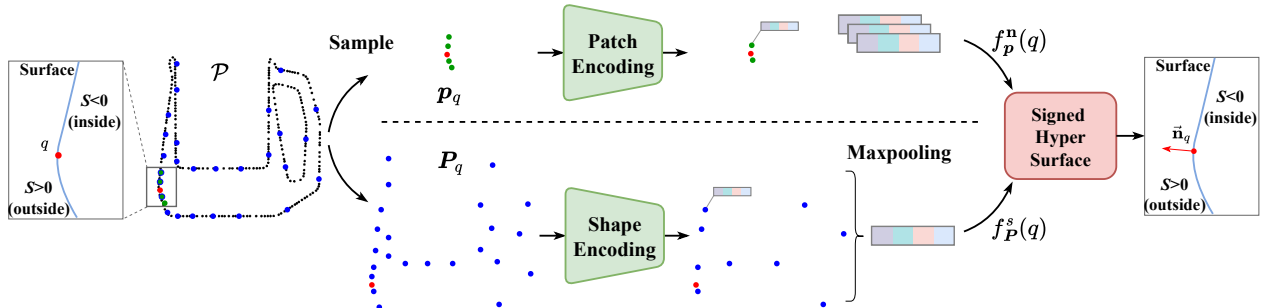


Figure 2. The learning pipeline of the signed hyper surfaces for oriented normal estimation.

through end-to-end deep networks. These methods focus on learning a general mapping from point clouds to normals and neglect the underlying surface distribution for normal orientation, leading to a sub-optimal solution.

3. Preliminary

In mathematics, an explicit representation in Euclidean space expresses the z coordinate of a point p in terms of the x and y : $z = f(x, y)$. Such a surface is called an explicit surface, also called a height field. Another symmetric representation is $F(x, y, z) = 0$, where F implicitly defines a locus called an implicit surface, also called a scalar field [7]. The implicit surface is a zero iso-surface of F , *i.e.*, the point set $\{p \in \mathbb{R}^3 : F(p) = 0\}$ is a surface implicitly defined by F . The explicit surface is usually used in surface fitting-based normal estimation, such as jet fitting [10], while the implicit surface is widely used in surface reconstruction. Generally, an explicit surface, *i.e.*, $z = f(x, y)$, can always be rewritten as an implicit surface, *i.e.*, $F(x, y, z) = z - f(x, y) = 0$. These two surface representations have the same tangent plane at a given point, where the normal is defined. See supplementary for details.

3.1. Explicit Surface Fitting

We employ the widely used n -jet surface model [10] to briefly review the explicit surface fitting for normal estimation. It represents the surface by a polynomial function $J_n : \mathbb{R}^2 \rightarrow \mathbb{R}$, which maps a coordinate (x, y) to its height z in the tangent space by

$$z = J_{\alpha, n}(x, y) = \sum_{k=0}^n \sum_{j=0}^k \alpha_{k-j, j} x^{k-j} y^j, \quad (1)$$

where α is the coefficient vector that defines the surface function. In order to find the optimal solution, the least squares approximation strategy is usually adopted to minimize the sum of the square errors between the (ground-truth) height and the jet value over a point set $\{\mathbf{p}_i\}_{i=1}^N$,

$$J_{\alpha, n}^* = \underset{\alpha}{\operatorname{argmin}} \sum_{i=1}^N \|z_i - J_{\alpha, n}(x_i, y_i)\|^2. \quad (2)$$

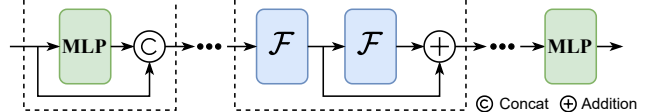


Figure 3. Feature encoding network in patch and shape encoding.

If $\alpha = (\alpha_{0,0}, \alpha_{1,0}, \alpha_{0,1}, \dots, \alpha_{0,n})$ is solved, then the normal at point p on the fitted surface is computed by

$$\mathbf{n}_p = h(\alpha) = (-\alpha_{1,0}, -\alpha_{0,1}, 1) / \sqrt{1 + \alpha_{1,0}^2 + \alpha_{0,1}^2}. \quad (3)$$

3.2. Implicit Surface Learning

In recent years, many learning-based approaches have been proposed to represent surfaces by implicit functions, such as signed distance function (SDF) [41] and occupancy function [36]. The signed (or oriented) distance function is the shortest distance of a given point $p = (x_0, y_0, z_0)$ to the closest surface S in a metric space, with the sign determined by whether the point is inside ($F(p) < 0$) or outside ($F(p) > 0$) of the surface. The underlying surface is implicitly represented by the iso-surface of $F(p) = 0$. In the surface reconstruction task, a deep network is usually adopted to encode a 3D shape into a latent code, which is fed into a decoder together with query points to predict signed distances. If an implicit surface function is continuous and differentiable, the formula of tangent plane at a regular point p (gradient is non-null) is $F'_x(p)(x - x_0) + F'_y(p)(y - y_0) + F'_z(p)(z - z_0) = 0$ and its normal (*i.e.*, perpendicular) is $\mathbf{n}_p = \nabla F(p)$.

4. Method

As shown in Fig. 2, we propose to implicitly learn signed hyper surfaces in the feature space for estimating oriented normals. In the following sections, we first introduce the representation of signed hyper surfaces by combining the characteristics of the above two surface representations. Then, we design an attention-weighted normal prediction module to deliver the oriented normals of query points from signed hyper surfaces. Finally, we introduce how to learn this new surface representation from patch encoding and shape encoding using our designed loss functions.

324
325
326
327
328
329
330

4.1. Signed Hyper Surface

The implicit surface $F(x, y, z) = z - f(x, y) = 0$ can be formulated as a more general format $F(z_1, z_2) = z_1 - z_2 = 0$. Similarly, the signed hyper surface is implicitly learned by taking the latent encodings of point clouds as inputs and outputting an approximation of the surface in feature space,

$$f_S(\chi) \approx \mathcal{E}_\theta(\chi | z_1, z_2), \quad z_1 = e_\varphi(\mathbf{P}_\chi^1), \quad z_2 = e_\psi(\mathbf{P}_\chi^2), \quad (4)$$

where \mathcal{E} is implemented by a neural network with parameter θ that is conditioned on two latent vectors $z_1, z_2 \in \mathbb{R}^c$, which are extracted from point clouds by the encoders e_φ and e_ψ , respectively. \mathbf{P}_χ^1 and \mathbf{P}_χ^2 are subsample sets of the raw point cloud \mathcal{P} , *e.g.*, point cloud patches around a given point χ .

Similar with existing unoriented normal estimation methods [5, 17, 32, 58], we use a local patch \mathbf{p}_q to capture the local geometry for accurately describing the surface pattern around a query point q ,

$$f_p^\mathbf{n}(q) = \mathcal{E}_\theta^\mathbf{n}(q | z_q^\mathbf{n}), \quad z_q^\mathbf{n} = e_\varphi(\mathbf{p}_q). \quad (5)$$

Since the interior/exterior of a surface cannot be determined reliably from a local patch, we take a global subsample set \mathbf{P}_q from the point cloud \mathcal{P} to provide additional information to estimate the sign at point q ,

$$f_P^s(q) = \text{sgn}(g^s(q)) = \text{sgn}(\mathcal{E}_\theta^s(q | z_q^s)), \quad z_q^s = e_\psi(\mathbf{P}_q), \quad (6)$$

where $\text{sgn}(\cdot)$ is signum function, $g^s(q)$ denotes logit of the probability that q has a positive sign. Thus, the signed hyper surface function at point q is formulated as

$$f_S(q) = f_p^\mathbf{n}(q) \cdot f_P^s(q) = \mathcal{E}_\theta^{\mathbf{n}, s}(q | z_q^\mathbf{n}, z_q^s). \quad (7)$$

Different from the surface reconstruction task that learns SDF by representing a surface as the zero-set of the SDF, we do not learn a distance field of points with respect to the underlying surface.

4.2. Oriented Normal Estimation

To simplify notations, we denote $\mathcal{E}_\theta^{\mathbf{n}, s}(q | z_q^\mathbf{n}, z_q^s)$ as $\mathcal{S}_\theta(\mathcal{X}, \mathcal{Y})$, where $z_q^\mathbf{n} = \mathcal{X} \in \mathbb{R}^c$ and $z_q^s = \mathcal{Y} \in \mathbb{R}^c$ are high dimensional latent vectors. According to the explicit surface fitting in Sec. 3.1, we formulate the signed hyper surface $\mathcal{S}_\theta : \mathbb{R}^{2c} \rightarrow \mathbb{R}^c$ as a feature-based polynomial function [32]

$$\mathcal{S}_{\theta, \mu}(\mathcal{X}, \mathcal{Y}) = \sum_{k=0}^{\mu} \sum_{j=0}^k \theta_{k-j, j} \mathbf{x}_{k-j} \mathbf{y}_j = \theta [\mathcal{X} : \mathcal{Y}], \quad (8)$$

where $[\cdot : \cdot]$ means the feature fusion through concatenation, μ denotes the number of fused items.

Similar with Eq. (2), the bivariate function $\mathcal{S}_{\theta, \mu}(\mathcal{X}, \mathcal{Y})$ aims to map a feature pair $(\mathcal{X}_i, \mathcal{Y}_i)$ to their ground-truth value $\mathcal{Z}_i = \hat{\mathcal{S}}(\mathcal{X}_i, \mathcal{Y}_i) \in \mathbb{R}^c$ in the feature space, *i.e.*,

$$\mathcal{S}_{\theta, \mu}^* = \underset{\theta, \mu}{\operatorname{argmin}} \sum_{i=1}^N \|\mathcal{Z}_i - \mathcal{S}_{\theta, \mu}(\mathcal{X}_i, \mathcal{Y}_i)\|^2. \quad (9)$$

378

379

380

381

382

383

384

385

386

387

388

389

390

391

392

393

394

395

396

397

398

399

400

401

402

403

404

405

406

407

408

409

410

411

412

413

414

415

416

417

418

419

420

421

422

423

424

425

426

427

428

429

430

431

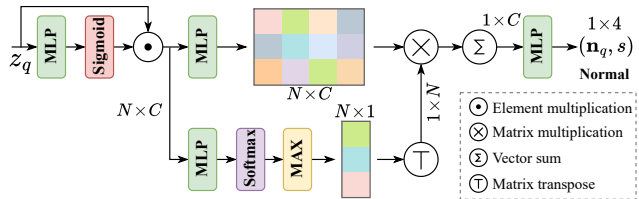


Figure 4. Attention-weighted normal prediction module.

We solve the oriented normal $\vec{\mathbf{n}}$ from signed hyper surfaces using a function \mathcal{H} ,

$$\mathcal{S}_{\theta, \mu}^* = \underset{\theta, \mu}{\operatorname{argmin}} \sum_{i=1}^N \|\mathcal{H}(\mathcal{Z}_i) - \mathcal{H}(\mathcal{S}_{\theta, \mu}(\mathcal{X}_i, \mathcal{Y}_i))\|^2. \quad (10)$$

Finally, the oriented normal is optimized by

$$\mathcal{S}_{\theta, \mu}^* = \underset{\theta, \mu}{\operatorname{argmin}} \sum_{i=1}^N \|\hat{\vec{\mathbf{n}}}_i - \vec{\mathbf{n}}_i\|^2. \quad (11)$$

Attention-weighted normal prediction $\mathcal{H} : \mathbb{R}^c \rightarrow \mathbb{R}^4$.

As shown in Fig. 4, we use an attention mechanism to recover the oriented normal $\vec{\mathbf{n}}_q$ of the query point q from c -dimensional fused surface embedding z_q ,

$$(\dot{\vec{\mathbf{n}}}_q, s) = \mathcal{O}(\mathcal{V}(o_q) \otimes \text{MAX}\{\text{softmax}_{\mathcal{N}_q}(\mathcal{Q}_j(o_q)_{j=1}^m)\}), \quad (12)$$

where $o_q = \tau \cdot z_q$, $\tau = \text{sigmoid}(\mathcal{I}(z_q))$. $\mathcal{O}, \mathcal{V}, \mathcal{Q}$ and \mathcal{I} are MLPs. $m = 64$ is the feature dimension size. First, a multi-head strategy is adopted to deliver m relative weights $\mathcal{Q}_j(o_q)$, which are normalized by softmax over neighbors \mathcal{N}_q into positive interpolation weights. Then, the feature maxpooling $\text{MAX}\{\cdot\}$ is performed to produce attention weights for each point. Meanwhile, the feature embedding o_q is refined through another branch \mathcal{V} and modulated as the weighted sum through matrix multiplication. Finally, the normal and its sign (*i.e.*, orientation) $\vec{\mathbf{n}}_q = (\mathbf{n}_q \in \mathbb{R}^3, s \in \mathbb{R})$ is predicted as a 4D vector, and $\mathbf{n}_q = \dot{\vec{\mathbf{n}}}_q / \|\dot{\vec{\mathbf{n}}}_q\|$.

4.3. Patch Encoding

Given a neighborhood point patch \mathbf{p}_q of the query point, our local latent code extraction layer \mathcal{F} is formulated as

$$\vec{\mathbf{z}}_i^\mathbf{n} = \mathcal{A} \left(\mathcal{B} \left(\text{MAX}\{\mathcal{C}(w_j \cdot z_j^\mathbf{n})\}_{j=1}^{N_l}\right), z_i^\mathbf{n} \right), \quad (13)$$

where $i = 1, \dots, N_{l+1}$, l is the neighborhood scale index and $N_{l+1} \leqslant N_l$. $z_i^\mathbf{n} = \mathcal{D}(p_i)$, $p_i \in \mathbf{p}_q$ is the per-point feature in the patch. $\mathcal{A}, \mathcal{B}, \mathcal{C}$ and \mathcal{D} are MLPs. $\text{MAX}\{\cdot\}$ denotes the feature maxpooling over N_l -nearest neighbors of the query point q . w is a distance-based weight given by

$$w_i = \frac{\beta_i}{\sum_{i=1}^N \beta_i}, \quad \beta_i = \text{sigmoid}(\gamma_1 - \gamma_2 \|p_i - q\|_2), \quad (14)$$

where γ_1 and γ_2 are learnable parameters with an initial value of 1.0. The weight w makes the layer focus on the point p_i which is closer to the query point q . As shown in Fig. 3, we stack two layers \mathcal{F} to form a block, which is further stacked to build our patch feature encoder e_φ .

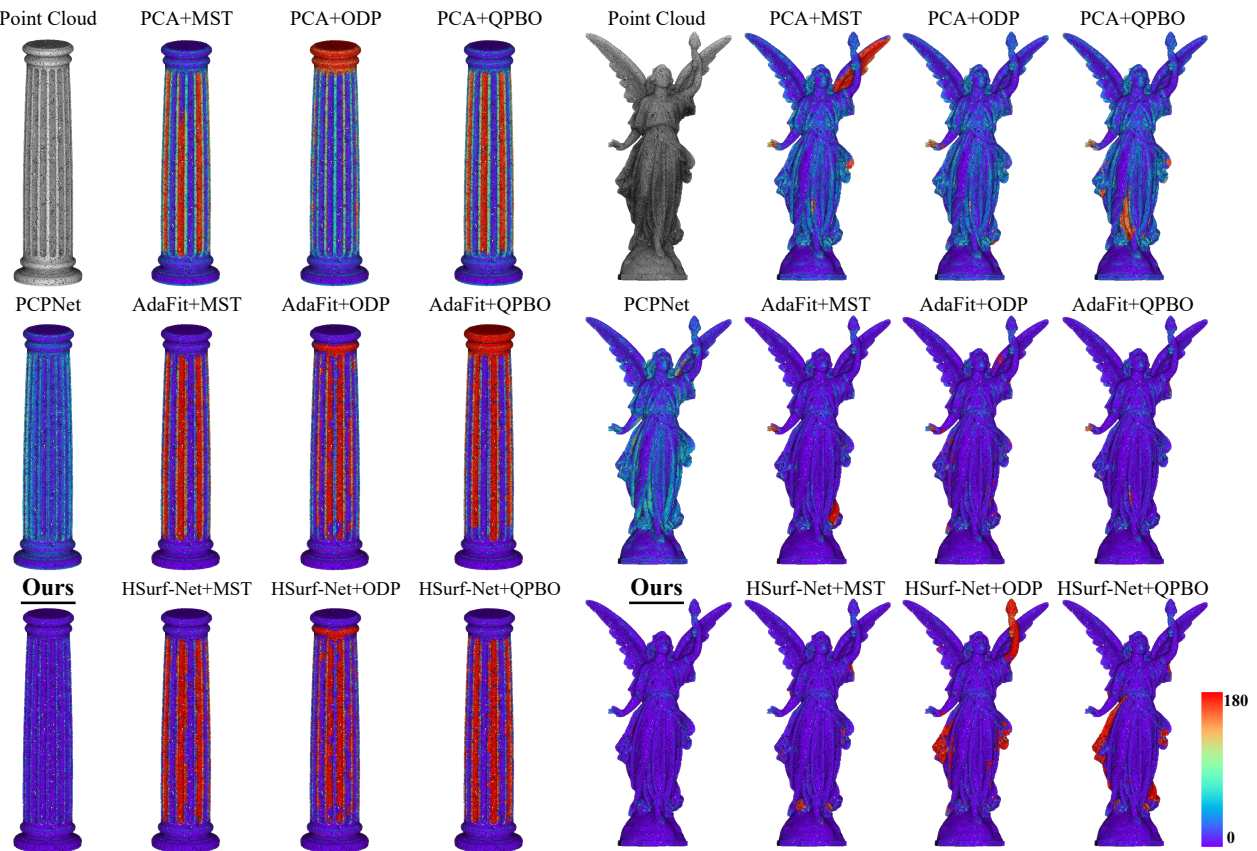


Figure 5. Visualization of the oriented normal error on datasets PCPNet (left) and FamousShape (right). The angle error is mapped to a heatmap ranging from 0° to 180° . The purple color indicates the same direction as the ground-truth, while the red color is the opposite.

4.4. Shape Encoding

Since the global subsample set $\mathcal{P}_q = \{p_i\}_{i=1}^{N_P}$ can be seen as a patch with points distributed globally on the shape surface, we adopt a similar network architecture with the patch feature encoder to get the global latent code z_q^s . To obtain \mathcal{P}_q , we use a probability-based sampling strategy [14], which brings more points closer to the query point q . It samples points according to a density gradient that decreases with increasing distance from the point q . Moreover, we find that adding more points from random sampling brings better results. Then, the gradient of a point is calculated by

$$v(p_i) = \begin{cases} \left[1 - 1.5 \frac{\|p_i - q\|_2}{\max_{p_j \in \mathcal{P}} \|p_j - q\|_2} \right]_0^{1.0} & \\ 1 & \text{if } i \in \mathcal{R} \end{cases} \quad (15)$$

where $[\cdot]_0^{1.0}$ indicates value clamping. \mathcal{R} is a random sample index set of \mathcal{P} with $N_P/1.5$ items. Finally, the sampling probability of a point $p_i \in \mathcal{P}$ is $\rho(p_i) = v(p_i) / \sum_{p_j \in \mathcal{P}} v(p_j)$.

Feature fusion. In order to allow each point in the local patch to have global information and determine the normal orientation, we first use the maxpooling and repetition operation to make the output global latent code has the same dimension as the local latent code. Then, the two kinds of

codes are fused by concatenation, *i.e.*, $[z_q^n : z_q^s]$ in Eq. (8).

4.5. Loss Functions

For the query point q , we constrain its unoriented normal and normal sign (*i.e.*, orientation), respectively. To learn an accurate unoriented normal, we employ the ground-truth $\hat{\mathbf{n}}_q$ to calculate a normal vector \sin loss [5]

$$\mathcal{L}_{\sin} = \|\mathbf{n}_q \times \hat{\mathbf{n}}_q\|. \quad (16)$$

For the normal orientation, we adopt the binary cross entropy H [14] to calculate a sign classification loss

$$\mathcal{L}_{sgn} = H(\sigma(g^s(q)), [f_S(q) > 0]), \quad (17)$$

where σ is a logistic function that converts the sign logits to probabilities. $[f_S(q) > 0]$ is 1 if the estimated normal faces the outward of surface S and 0 otherwise. Our method achieves a significant performance boost by dividing the oriented normal estimation into unoriented normal regression and its sign classification, instead of directly regressing the oriented normals of query points (see Sec. 5.3).

For the oriented normals of neighbor points $p_i \in \mathcal{P}_q$, we compute a weighted mean square error (MSE)

$$\mathcal{L}_{mse} = \frac{1}{N} \sum_{i=1}^N \tau_i \|\vec{\mathbf{n}}_i - \hat{\vec{\mathbf{n}}}_i\|^2, \quad (18)$$

540

Table 1. Unoriented normal RMSE results on datasets PCPNet and FamousShape. * means the source code is uncompleted or unavailable.

594

Category	PCPNet Dataset						FamousShape Dataset							
	Noise				Density		Average	Noise				Average		
	None	0.12%	0.6%	1.2%	Stripe	Gradient		None	0.12%	0.6%	1.2%			
Jet [10]	12.35	12.84	18.33	27.68	13.39	13.13	16.29	20.11	20.57	31.34	45.19	18.82	18.69	25.79
PCA [19]	12.29	12.87	18.38	27.52	13.66	12.81	16.25	19.90	20.60	31.33	45.00	19.84	18.54	25.87
PCPNet [17]	9.64	11.51	18.27	22.84	11.73	13.46	14.58	18.47	21.07	32.60	39.93	18.14	19.50	24.95
Zhou <i>et al.</i> * [56]	8.67	10.49	17.62	24.14	10.29	10.66	13.62	-	-	-	-	-	-	-
Nesti-Net [6]	7.06	10.24	17.77	22.31	8.64	8.95	12.49	11.60	16.80	31.61	39.22	12.33	11.77	20.55
Lenssen <i>et al.</i> [29]	6.72	9.95	17.18	21.96	7.73	7.51	11.84	11.62	16.97	30.62	39.43	11.21	10.76	20.10
DeepFit [5]	6.51	9.21	16.73	23.12	7.92	7.31	11.80	11.21	16.39	29.84	39.95	11.84	10.54	19.96
MTRNet* [9]	6.43	9.69	17.08	22.23	8.39	6.89	11.78	-	-	-	-	-	-	-
Refine-Net [55]	5.92	9.04	16.52	22.19	7.70	7.20	11.43	-	-	-	-	-	-	-
Zhang <i>et al.</i> * [53]	5.65	9.19	16.78	22.93	6.68	6.29	11.25	9.83	16.13	29.81	39.81	9.72	9.19	19.08
Zhou <i>et al.</i> * [57]	5.90	9.10	16.50	22.08	6.79	6.40	11.13	-	-	-	-	-	-	-
AdaFit [58]	5.19	9.05	16.45	21.94	6.01	5.90	10.76	9.09	15.78	29.78	38.74	8.52	8.57	18.41
GraphFit [31]	5.21	8.96	16.12	21.71	6.30	5.86	10.69	8.91	15.73	29.37	38.67	9.10	8.62	18.40
HSurf-Net [32]	4.17	8.78	16.25	21.61	4.98	4.86	10.11	7.59	15.64	29.43	38.54	7.63	7.40	17.70
Ours	3.95	8.55	16.13	21.53	4.91	4.67	9.96	7.41	15.34	29.33	38.56	7.74	7.28	17.61

where the neighborhood point normals $\vec{n} = \delta(z_q)$ are predicted from the surface embedding z_q by an MLP layer $\delta : \mathbb{R}^c \rightarrow \mathbb{R}^3$. Furthermore, we add a loss term according to coplanarity [53] to facilitate the learning of τ in Eq. (12),

$$\mathcal{L}_\tau = \frac{1}{N} \sum_{i=1}^N (\tau_i - \hat{\tau}_i)^2, \quad \hat{\tau}_i = \exp \left(-\frac{(p_i \cdot \hat{n}_q)^2}{\xi^2} \right), \quad (19)$$

where $\xi = \max(0.05^2, 0.3 \sum_{i=1}^N (p_i \cdot \hat{n}_q)^2 / N)$. In summary, our final training loss for oriented normal estimation is

$$\mathcal{L} = \lambda_1 \mathcal{L}_{sin} + \lambda_2 \mathcal{L}_{sgn} + \lambda_3 \mathcal{L}_{mse} + \lambda_4 \mathcal{L}_\tau, \quad (20)$$

where $\lambda_1 = 0.1$, $\lambda_2 = 0.1$, $\lambda_3 = 0.5$ and $\lambda_4 = 1.0$ are factors.

5. Experiments

Implementation. We only train our network model on the PCPNet shape dataset [17], which provides the ground-truth normals with consistent orientation (outward of the surface). We follow the same train/test data split and data processing as in [5, 17, 32, 58]. For patch encoding, we randomly select a query point from the shape point cloud and search its 700 neighbors to form a patch. For shape encoding, we sample $N_P = 1200$ points from the shape point cloud according to the sampling probability. The Adam optimizer is adopted with an initial learning rate of 9×10^{-4} which is decayed to $1/5$ of the latest value at epochs $\{400, 600, 800\}$. The model is trained on an NVIDIA 2080 Ti GPU with a batch size of 145 and epochs of 800.

Dataset. Due to the lack of relevant datasets and the relatively simple test shapes of the PCPNet dataset [17], we further collect shapes with complex structures from other public datasets, such as the Famous dataset [14] and the Stanford 3D Scanning Repository [12]. We follow the same pre-processing steps as the PCPNet dataset to conduct data augmentation, *e.g.*, adding Gaussian noise with different levels

(0.12%, 0.6% and 1.2%) and uneven sampling (stripe and gradient). The ground-truth oriented normals are extracted from mesh data and used for evaluation. We call this new dataset *FamousShape* and it will be publicly available.

Metrics. We use the angle Root Mean Squared Error (RMSE) to evaluate the estimated normals and the Area Under the Curve (AUC) to show the error distribution [17, 32, 58]. Note that for the baseline methods, we flip their oriented normals if more than half of the normals face inward.

5.1. Unoriented Normal Comparison

We directly use our *oriented* normal estimation results to compare with baseline methods that are designed for estimating *unoriented* normals, such as the traditional methods PCA [19] and Jet [10], the learning-based surface fitting methods DeepFit [5] and AdaFit [58], and the learning-based regression methods Nesti-Net [6] and HSurf-Net [32]. As shown in Table 1, we report quantitative comparison results with the baselines in terms of normal angle RMSE on two datasets, PCPNet and FamousShape. On the PCPNet dataset, our method achieves the best performance under all noise levels and density variations. On our FamousShape dataset, our method achieves the best performance under most metrics and has the best average result.

5.2. Oriented Normal Comparison

We compare our approach for *oriented* normal estimation with various baseline methods, such as PCPNet [17] and DPGO [49]. In addition, we choose three *unoriented* normal estimation methods (PCA [19], AdaFit [58] and HSurf-Net [32]) and three normal orientation methods (MST [19], QPBO [44] and ODP [37]), and make different combinations of them to form two-stage pipelines for estimating oriented normals, such as PCA+MST. Among

648

Table 2. Oriented normal RMSE results on datasets PCPNet and FamousShape. * means the source code is uncompleted.

702

649

Category	PCPNet Dataset								FamousShape Dataset										
	Noise				Density				Average	Noise				Density				Average	
	None	0.12%	0.6%	1.2%	Stripe	Gradient	Average	None		0.12%	0.6%	1.2%	Stripe	Gradient	None	0.12%	1.2%		
PCA [19]+MST [19]	19.05	30.20	31.76	39.64	27.11	23.38	28.52	35.88	41.67	38.09	60.16	31.69	35.40	40.48	702	703	704	705	706
PCA [19]+QPBO [44]	18.55	21.61	30.94	39.54	23.00	25.46	26.52	32.25	39.39	41.80	61.91	36.69	35.82	41.31	707	708	709	710	711
PCA [19]+ODP [37]	28.96	25.86	34.91	51.52	28.70	23.00	32.16	30.47	31.29	41.65	84.00	39.41	30.72	42.92	712	713	714	715	716
AdaFit [58]+MST [19]	27.67	43.69	48.83	54.39	36.18	40.46	41.87	43.12	39.33	62.28	60.27	45.57	42.00	48.76	717	718	719	720	721
AdaFit [58]+QPBO [44]	26.41	24.17	40.31	48.76	27.74	31.56	33.16	27.55	37.60	69.56	62.77	27.86	29.19	42.42	722	723	724	725	726
AdaFit [58]+ODP [37]	26.37	24.86	35.44	51.88	26.45	20.57	30.93	41.75	39.19	44.31	72.91	45.09	42.37	47.60	727	728	729	730	731
HSurf-Net [32]+MST [19]	29.82	44.49	50.47	55.47	40.54	43.15	43.99	54.02	42.67	68.37	65.91	52.52	53.96	56.24	732	733	734	735	736
HSurf-Net [32]+QPBO [44]	30.34	32.34	44.08	51.71	33.46	40.49	38.74	41.62	41.06	67.41	62.04	45.59	43.83	50.26	737	738	739	740	741
HSurf-Net [32]+ODP [37]	26.91	24.85	35.87	51.75	26.91	20.16	31.07	43.77	43.74	46.91	72.70	45.09	43.98	49.37	746	747	748	749	750
PCPNet [17]	33.34	34.22	40.54	44.46	37.95	35.44	37.66	40.51	41.09	46.67	54.36	40.54	44.26	44.57	754	755	756	757	758
DPGO* [49]	23.79	25.19	35.66	43.89	28.99	29.33	31.14	-	-	-	-	-	-	-	759	760	761	762	763
Ours	10.28	13.23	25.40	35.51	16.40	17.92	19.79	21.63	25.96	41.14	52.67	26.39	28.97	32.79	764	765	766	767	768

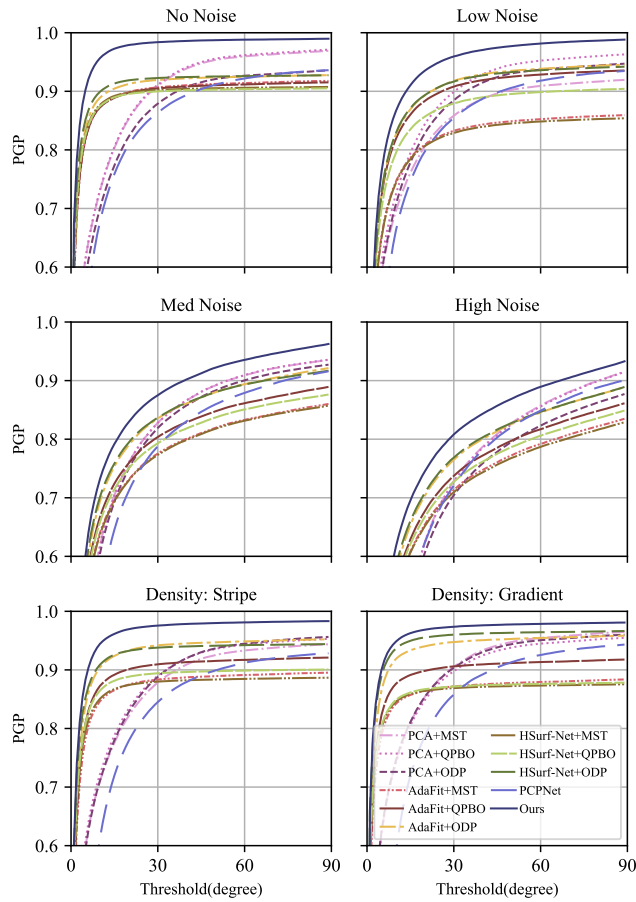


Figure 6. Oriented normal AUC on the PCPNet dataset. It shows the percentage of correctly estimated normals (PGP) for a given angle threshold. Our method has the best value for all thresholds.

the baselines, PCA is a widely used traditional method, AdaFit is a representative surface fitting-based method, and HSurf-Net is a regression-based method and has the state-of-the-art performance for *unoriented* normal estimation. We use the original implementation of QPBO and ODP, and the implementation of MST in [46]. In Table 2, we show quantitative comparison results on datasets PCPNet

and FamousShape. We can see that our method provides the most accurate normals under almost all noise levels and density variations for both datasets, and achieves huge performance gains in terms of average results compared to all baselines. From the experimental results, we find that the propagation-based normal orientation methods have significantly varied results when dealing with unoriented normal inputs from different estimation methods, such as PCA+MST and AdaFit+MST. A visual comparison of the normal errors is shown in Fig. 5. The error distributions of various methods are illustrated in Fig. 6.

KITTI dataset. To verify the generalization ability of our method on LiDAR point clouds of outdoor scenes, we test directly on the KITTI dataset [15] with the model trained on the PCPNet dataset. We only report qualitative results on this dataset as it does not provide the ground-truth normals. In Fig. 7, we use the Poisson surface reconstruction algorithm [26] to generate surfaces using oriented normals estimated by different methods. As can be seen, compared to the baselines, our estimated normals facilitate the algorithm to reconstruct surfaces that can more accurately depict the spatial structure and distribution of real scenes.

5.3. Ablation Studies

We provide ablation results for oriented normal estimation in Table 3 (a)-(d), which are discussed as follows.

(a) Feature encoding. (1) We realize the oriented normal estimation without using the patch encoding or the shape encoding. (2) The distance-based weight w is not used in both patch encoding and shape encoding.

(b) Module \mathcal{H} . The attention-weighted normal prediction module \mathcal{H} is replaced with simple MLP layers.

(c) Loss $\mathcal{L}_{sin}, \mathcal{L}_{sgn}$. In our pipeline, we regress the unoriented normal and its sign of the query point q , and constrain them in loss functions \mathcal{L}_{sin} and \mathcal{L}_{sgn} , respectively. Here, we alternatively directly predict the oriented normal \vec{n}_q from surface embedding and compute its MSE loss.

(d) Point sampling. In the shape encoding, we obtain a

756

Table 3. Ablation studies for oriented normals on the PCPNet dataset. The last column is the average results under the unoriented metric.

	Ablation	Feat. Enco.	Module \mathcal{H}	Loss	Point Samp.	None	Noise 0.12%	Noise 0.6%	Noise 1.2%	Density Stripe	Density Gradient	Oriented Average	Unoriented Average
(a)	w/o patch encoding		✓	✓	✓	35.19	42.23	55.59	61.38	38.92	41.49	45.80	18.83
	w/o shape encoding		✓	✓	✓	69.72	64.37	81.87	77.07	74.84	90.35	76.37	14.94
	w/o weight w		✓	✓	✓	11.15	14.32	26.49	36.03	17.99	26.03	22.00	10.48
(b)	w/o module \mathcal{H}	✓		✓	✓	12.08	14.53	25.87	35.88	18.45	31.84	23.11	10.24
(c)	w/o $\mathcal{L}_{sin}, \mathcal{L}_{sgn}$	✓	✓		✓	23.86	25.55	34.13	42.48	32.42	41.30	33.29	20.23
(d)	w/o density gradient	✓	✓	✓		12.10	18.25	28.05	38.15	19.79	28.09	24.07	10.00
	w/o random sample	✓	✓	✓		11.01	13.79	25.64	35.86	17.22	25.71	21.54	9.94
	$\zeta=1/2$	✓	✓	✓		10.99	14.04	25.66	35.78	17.73	37.82	23.67	9.92
	$\zeta=1/3$	✓	✓	✓		13.27	15.42	26.82	37.16	17.52	28.11	23.05	9.95
	$N_P=1100$	✓	✓	✓		10.67	14.21	25.54	35.97	16.80	26.98	21.69	9.99
	$N_P=1300$	✓	✓	✓		12.44	14.53	25.93	35.79	18.40	19.85	21.16	9.98
	Final	✓	✓	✓	✓	10.28	13.23	25.40	35.51	16.40	17.92	19.79	9.96

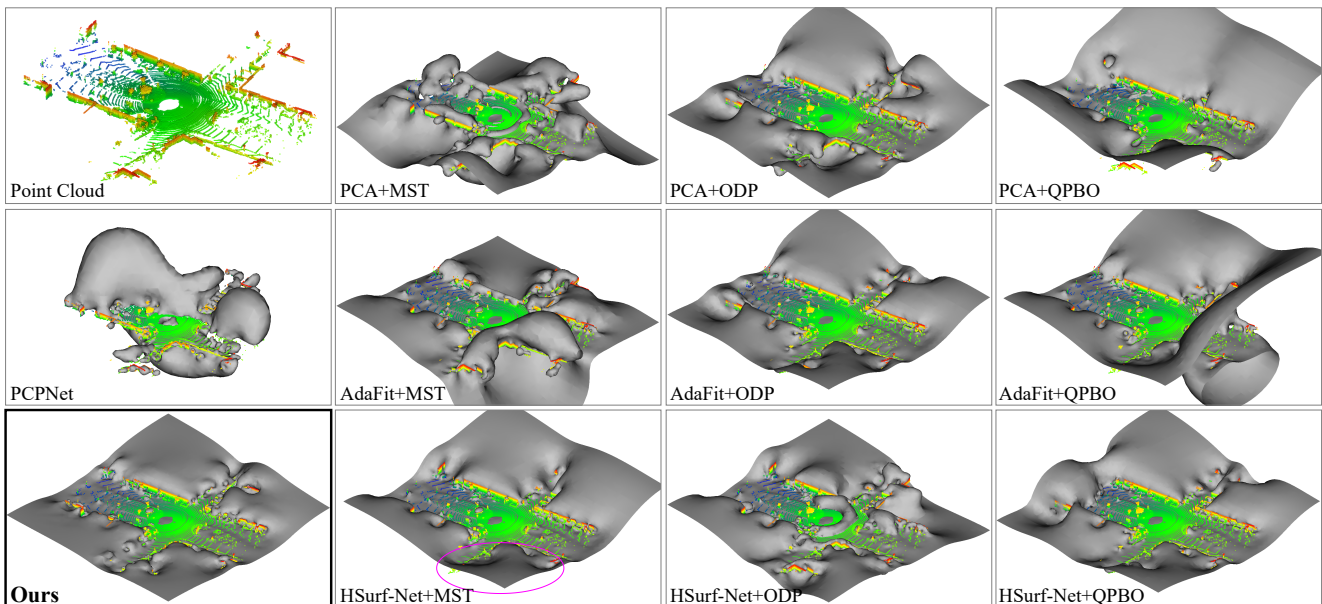


Figure 7. The reconstructed surfaces using oriented normals estimated by different methods on the KITTI dataset.

global point set P_q by a probability-based sampling strategy as in Eq. (15), which includes density gradient term and random sample term. The point set P_q includes $N_P=1200$ points, and the ratio of randomly sampled points is $\zeta = 1/1.5$. (1) We only adopt one of the two terms in Eq. (15) for point sampling, e.g., ‘w/o density gradient’ means all points are randomly sampled. (2) The ratio ζ is changed to 1/2 and 1/3. (3) The number N_P is set to 1100 and 1300.

From Table 3, we can conclude that both patch encoding and shape encoding are vital for learning accurate oriented and unoriented normals in our pipeline. The adoption of the weight w and the attention-weighted normal prediction module \mathcal{H} effectively improves the algorithm’s performance. Compared to directly predicting the oriented normal \vec{n}_q , solving it separately by learning signed hyper surface is significantly better. The combination of the density gradient term and the random sample term in sampling can produce better results than either one alone. The proportion and number of points in the sampling of shape encoding

have a significant positive effect on oriented normals, but very little on unoriented normals.

6. Conclusion

In this work, we formulate the oriented normal estimation of point clouds as the learning of signed hyper surfaces. We first review the explicit surface fitting and the implicit surface learning, and derive the formulation of the signed hyper surfaces from their inspiration. Then, we propose to use an attention-weighted normal prediction module to recover the normal and its sign of the query point from the embedding of the signed hyper surfaces. Finally, we introduce how such surfaces can be learned from the patch encoding and shape encoding using the designed loss functions. We conduct extensive evaluation and ablation experiments to report the state-of-the-art performance and justify the effectiveness of our designs. We show that the oriented normal estimation is tightly coupled with the surface reconstruction, which is an area to be explored in future work.

864

References

865

866

867

868

869

870

871

872

873

874

875

876

877

878

879

880

881

882

883

884

885

886

887

888

889

890

891

892

893

894

895

896

897

898

899

900

901

902

903

904

905

906

907

908

909

910

911

912

913

914

915

916

917

- [1] Marc Alexa, Johannes Behr, Daniel Cohen-Or, Shachar Fleishman, David Levin, and Claudio T Silva. Point set surfaces. In *Proceedings Visualization, 2001. VIS'01.*, pages 21–29. IEEE, 2001. [2](#)
- [2] Pierre Alliez, David Cohen-Steiner, Yiyi Tong, and Mathieu Desbrun. Voronoi-based variational reconstruction of un-oriented point sets. In *Symposium on Geometry Processing*, volume 7, pages 39–48, 2007. [2](#)
- [3] Nina Amenta and Marshall Bern. Surface reconstruction by voronoi filtering. *Discrete & Computational Geometry*, 22(4):481–504, 1999. [2](#)
- [4] Samir Aroudj, Patrick Seemann, Fabian Langguth, Stefan Guthe, and Michael Goesele. Visibility-consistent thin surface reconstruction using multi-scale kernels. *ACM Transactions on Graphics*, 36(6):1–13, 2017. [2](#)
- [5] Yizhak Ben-Shabat and Stephen Gould. DeepFit: 3D surface fitting via neural network weighted least squares. In *European Conference on Computer Vision*, pages 20–34. Springer, 2020. [1, 2, 4, 5, 6](#)
- [6] Yizhak Ben-Shabat, Michael Lindenbaum, and Anath Fischer. Nesti-Net: Normal estimation for unstructured 3D point clouds using convolutional neural networks. In *Proceedings of the IEEE Conference on Computer Vision and Pattern Recognition*, pages 10112–10120, 2019. [2, 6](#)
- [7] Jules Bloomenthal, Chandrajit Bajaj, Jim Blinn, Marie-Paule Cani, Brian Wyvill, Alyn Rockwood, and Geoff Wyvill. *Introduction to implicit surfaces*. Morgan Kaufmann, 1997. [3](#)
- [8] Alexandre Boulch and Renaud Marlet. Deep learning for robust normal estimation in unstructured point clouds. In *Computer Graphics Forum*, volume 35, pages 281–290. Wiley Online Library, 2016. [2](#)
- [9] Junjie Cao, Hairui Zhu, Yunpeng Bai, Jun Zhou, Jinshan Pan, and Zhixun Su. Latent tangent space representation for normal estimation. *IEEE Transactions on Industrial Electronics*, 69(1):921–929, 2021. [2, 6](#)
- [10] Frédéric Cazals and Marc Pouget. Estimating differential quantities using polynomial fitting of osculating jets. *Computer Aided Geometric Design*, 22(2):121–146, 2005. [2, 3, 6](#)
- [11] Yi-Ling Chen, Bing-Yu Chen, Shang-Hong Lai, and Tomoyuki Nishita. Binary orientation trees for volume and surface reconstruction from unoriented point clouds. In *Computer Graphics Forum*, volume 29, pages 2011–2019. Wiley Online Library, 2010. [2](#)
- [12] Brian Curless and Marc Levoy. A volumetric method for building complex models from range images. In *Proceedings of the 23rd Annual Conference on Computer Graphics and Interactive Techniques*, pages 303–312, 1996. [6](#)
- [13] Tamal K Dey and Samrat Goswami. Provable surface reconstruction from noisy samples. *Computational Geometry*, 35(1-2):124–141, 2006. [2](#)
- [14] Philipp Erler, Paul Guerrero, Stefan Ohrhallinger, Niloy J Mitra, and Michael Wimmer. Points2Surf: learning implicit surfaces from point clouds. In *European Conference on Computer Vision*, pages 108–124. Springer, 2020. [5, 6](#)

- [15] Andreas Geiger, Philip Lenz, and Raquel Urtasun. Are we ready for autonomous driving? the kitti vision benchmark suite. In *IEEE Conference on Computer Vision and Pattern Recognition*, pages 3354–3361. IEEE, 2012. [7](#)
- [16] Gaël Guennebaud and Markus Gross. Algebraic point set surfaces. In *ACM SIGGRAPH 2007 papers*. 2007. [2](#)
- [17] Paul Guerrero, Yanir Kleiman, Maks Ovsjanikov, and Niloy J Mitra. PCPNet: learning local shape properties from raw point clouds. In *Computer Graphics Forum*, volume 37, pages 75–85. Wiley Online Library, 2018. [2, 4, 6, 7](#)
- [18] Taisuke Hashimoto and Masaki Saito. Normal estimation for accurate 3D mesh reconstruction with point cloud model incorporating spatial structure. In *CVPR Workshops*, pages 54–63, 2019. [2](#)
- [19] Hugues Hoppe, Tony DeRose, Tom Duchamp, John McDonald, and Werner Stuetzle. Surface reconstruction from unorganized points. In *Proceedings of the 19th Annual Conference on Computer Graphics and Interactive Techniques*, pages 71–78, 1992. [1, 2, 6, 7](#)
- [20] Hui Huang, Dan Li, Hao Zhang, Uri Ascher, and Daniel Cohen-Or. Consolidation of unorganized point clouds for surface reconstruction. *ACM Transactions on Graphics*, 28(5):1–7, 2009. [2](#)
- [21] Zhiyang Huang, Nathan Carr, and Tao Ju. Variational implicit point set surfaces. *ACM Transactions on Graphics*, 38(4):1–13, 2019. [2](#)
- [22] Johannes Jakob, Christoph Buchenau, and Michael Guthe. Parallel globally consistent normal orientation of raw unorganized point clouds. In *Computer Graphics Forum*, volume 38, pages 163–173. Wiley Online Library, 2019. [2](#)
- [23] Sagi Katz, Ayellet Tal, and Ronen Basri. Direct visibility of point sets. In *ACM SIGGRAPH*, pages 24–es. 2007. [2](#)
- [24] Michael Kazhdan. Reconstruction of solid models from oriented point sets. In *Proceedings of the third Eurographics Symposium on Geometry Processing*, 2005. [1](#)
- [25] Michael Kazhdan, Matthew Bolitho, and Hugues Hoppe. Poisson surface reconstruction. In *Proceedings of the fourth Eurographics Symposium on Geometry Processing*, volume 7, 2006. [1](#)
- [26] Michael Kazhdan and Hugues Hoppe. Screened poisson surface reconstruction. *ACM Transactions on Graphics*, 32(3):1–13, 2013. [1, 7](#)
- [27] Sören König and Stefan Gumhold. Consistent propagation of normal orientations in point clouds. In *VMV*, pages 83–92, 2009. [1](#)
- [28] Carsten Lange and Konrad Polthier. Anisotropic smoothing of point sets. *Computer Aided Geometric Design*, 22(7):680–692, 2005. [2](#)
- [29] Jan Eric Lenssen, Christian Osendorfer, and Jonathan Masci. Deep iterative surface normal estimation. In *Proceedings of the IEEE/CVF Conference on Computer Vision and Pattern Recognition*, pages 11247–11256, 2020. [1, 2, 6](#)
- [30] David Levin. The approximation power of moving least-squares. *Mathematics of Computation*, 67(224):1517–1531, 1998. [2](#)
- [31] Keqiang Li, Mingyang Zhao, Huaiyu Wu, Dong-Ming Yan, Zhen Shen, Fei-Yue Wang, and Gang Xiong. GraphFit:

- 972 Learning multi-scale graph-convolutional representation for
973 point cloud normal estimation. *European Conference on*
974 *Computer Vision*, 2022. 1, 2, 6
- 975 [32] Qing Li, Yu-Shen Liu, Jin-San Cheng, Cheng Wang, Yi
976 Fang, and Zhizhong Han. HSurf-Net: Normal estimation
977 for 3D point clouds by learning hyper surfaces. *Advances in*
978 *Neural Information Processing Systems (NeurIPS)*, 2022. 1,
979 2, 4, 6, 7
- 980 [33] Denning Lu, Xuequan Lu, Yangxing Sun, and Jun Wang.
981 Deep feature-preserving normal estimation for point cloud
982 filtering. *Computer-Aided Design*, 125:102860, 2020. 2
- 983 [34] Víni cius Mello, Luiz Velho, and Gabriel Taubin. Estimating
984 the in/out function of a surface represented by points. In *Pro-
985 ceedings of the Eighth ACM Symposium on Solid Modeling and
986 Applications*, pages 108–114, 2003. 2
- 987 [35] Quentin Mérigot, Maks Ovsjanikov, and Leonidas J Guibas.
988 Voronoi-based curvature and feature estimation from point
989 clouds. *IEEE Transactions on Visualization and Computer
990 Graphics*, 17(6):743–756, 2010. 2
- 991 [36] Lars Mescheder, Michael Oechsle, Michael Niemeyer, Se-
992 bastian Nowozin, and Andreas Geiger. Occupancy Networks:
993 Learning 3D reconstruction in function space. In *Proceedings of the IEEE/CVF Conference on Computer
994 Vision and Pattern Recognition*, pages 4460–4470, 2019. 3
- 995 [37] Gal Metzler, Rana Hanocka, Denis Zorin, Raja Giryes,
996 Daniele Panozzo, and Daniel Cohen-Or. Orienting point
997 clouds with dipole propagation. *ACM Transactions on
998 Graphics*, 40(4):1–14, 2021. 1, 2, 6, 7
- 999 [38] Niloy J Mitra and An Nguyen. Estimating surface normals
1000 in noisy point cloud data. In *Proceedings of the Nineteenth
1001 Annual Symposium on Computational Geometry*, pages 322–
1002 328, 2003. 2
- 1003 [39] Patrick Mullen, Fernando De Goes, Mathieu Desbrun, David
1004 Cohen-Steiner, and Pierre Alliez. Signing the unsigned: Ro-
1005 bust surface reconstruction from raw pointsets. In *Computer
1006 Graphics Forum*, volume 29, pages 1733–1741. Wiley On-
1007 line Library, 2010. 2
- 1008 [40] A Cengiz Öztireli, Gael Guennebaud, and Markus Gross.
1009 Feature preserving point set surfaces based on non-linear
1010 kernel regression. In *Computer Graphics Forum*, volume 28,
1011 pages 493–501. Wiley Online Library, 2009. 2
- 1012 [41] Jeong Joon Park, Peter Florence, Julian Straub, Richard
1013 Newcombe, and Steven Lovegrove. DeepSDF: Learning
1014 continuous signed distance functions for shape representa-
1015 tion. In *Proceedings of the IEEE/CVF Conference on Com-
1016 puter Vision and Pattern Recognition*, pages 165–174, 2019.
1017 3
- 1018 [42] Mark Pauly, Markus Gross, and Leif P Kobbelt. Efficient
1019 simplification of point-sampled surfaces. In *IEEE Visualiza-
1020 tion, 2002. VIS 2002.*, pages 163–170. IEEE, 2002. 2
- 1021 [43] Riccardo Roveri, A Cengiz Öztireli, Ioana Pandele, and
1022 Markus Gross. PointProNets: Consolidation of point clouds
1023 with convolutional neural networks. In *Computer Graphics
1024 Forum*, volume 37, pages 87–99. Wiley Online Library,
1025 2018. 2
- 1026 [44] Nico Schertler, Bogdan Savchynskyy, and Stefan Gumhold.
1027 Towards globally optimal normal orientations for large point
1028 clouds. In *Computer Graphics Forum*, volume 36, pages
1029 197–208. Wiley Online Library, 2017. 1, 2, 6, 7
- 1030 [45] Lee M Seversky, Matt S Berger, and Lijun Yin. Harmonic
1031 point cloud orientation. *Computers & Graphics*, 35(3):492–
1032 499, 2011. 2
- 1033 [46] CloudCompare (version 2.12) [GPL software]. User docu-
1034 mentation. <http://www.cloudcompare.org>, 2022. 7
- 1035 [47] Christian Walder, Olivier Chapelle, and Bernhard Schölkopf.
1036 Implicit surface modelling as an eigenvalue problem. In *Pro-
1037 ceedings of the 22nd International Conference on Machine
1038 Learning*, pages 936–939, 2005. 2
- 1039 [48] Jun Wang, Zhouwang Yang, and Falai Chen. A variational
1040 model for normal computation of point clouds. *The Visual
1041 Computer*, 28(2):163–174, 2012. 2
- 1042 [49] Shiyao Wang, Xiuping Liu, Jian Liu, Shuhua Li, and
1043 Junjie Cao. Deep patch-based global normal orientation.
1044 *Computer-Aided Design*, page 103281, 2022. 2, 6, 7
- 1045 [50] Dong Xiao, Zuoqiang Shi, Siyu Li, Bailin Deng, and Bin
1046 Wang. Point normal orientation and surface reconstruction
1047 by incorporating isovalue constraints to poisson equation.
1048 *arXiv preprint arXiv:2209.15619*, 2022. 2
- 1049 [51] Hui Xie, Kevin T McDonnell, and Hong Qin. Surface recon-
1050 struction of noisy and defective data sets. In *IEEE Visualiza-
1051 tion*, pages 259–266. IEEE, 2004. 2
- 1052 [52] Minfeng Xu, Shiqing Xin, and Changhe Tu. Towards glob-
1053 ally optimal normal orientations for thin surfaces. *Computers
1054 & Graphics*, 75:36–43, 2018. 2
- 1055 [53] Jie Zhang, Jun-Jie Cao, Hai-Rui Zhu, Dong-Ming Yan, and
1056 Xiu-Ping Liu. Geometry guided deep surface normal estima-
1057 tion. *Computer-Aided Design*, 142:103119, 2022. 2, 6
- 1058 [54] Haoran Zhou, Honghua Chen, Yidan Feng, Qiong Wang,
1059 Jing Qin, Haoran Xie, Fu Lee Wang, Mingqiang Wei, and
1060 Jun Wang. Geometry and learning co-supported normal es-
1061 timation for unstructured point cloud. In *Proceedings of
1062 the IEEE/CVF Conference on Computer Vision and Pattern
1063 Recognition*, pages 13238–13247, 2020. 2
- 1064 [55] Haoran Zhou, Honghua Chen, Yingkui Zhang, Mingqiang
1065 Wei, Haoran Xie, Jun Wang, Tong Lu, Jing Qin, and Xiao-
1066 Ping Zhang. Refine-Net: Normal refinement neural network
1067 for noisy point clouds. *IEEE Transactions on Pattern Anal-
1068 sis and Machine Intelligence*, 2022. 2, 6
- 1069 [56] Jun Zhou, Hua Huang, Bin Liu, and Xiuping Liu. Normal
1070 estimation for 3D point clouds via local plane constraint and
1071 multi-scale selection. *Computer-Aided Design*, 129:102916,
1072 2020. 2, 6
- 1073 [57] Jun Zhou, Wei Jin, Mingjie Wang, Xiuping Liu, Zhiyang Li,
1074 and Zhaobin Liu. Improvement of normal estimation for
1075 point clouds via simplifying surface fitting. *arXiv preprint
1076 arXiv:2104.10369*, 2021. 2, 6
- 1077 [58] Runsong Zhu, Yuan Liu, Zhen Dong, Yuan Wang, Tengping
1078 Jiang, Wenping Wang, and Bisheng Yang. AdaFit: Rethink-
1079 ing learning-based normal estimation on point clouds. In
1075 *Proceedings of the IEEE/CVF International Conference on
1076 Computer Vision*, pages 6118–6127, 2021. 1, 2, 4, 6, 7